Field-Based Discretization of the 3-D Contrast Source Inversion Method Applied to Brain Stroke Microwave Imaging

Field-based Discretization of the 3-D Contrast Source Inversion Method applied to Brain Stroke Microwave Imaging

Valeria Mariano, *Member, IEEE*, Jorge A. Tobon Vasquez, *Member, IEEE*, David O. Rodriguez-Duarte, *Member, IEEE* and Francesca Vipiana, *Senior Member, IEEE*

***Abstract*—The contrast source inversion method is an iterative non-linear algorithm, and, in this paper, it works in combination with a finite element method solver for the reconstruction of the dielectric properties' distribution in the head with the aim to diagnose brain stroke. Here, the involved contrast source variables are discretized through a novel field-based discretization that allows a linear variation of the variables, leading to their more accurate description, and therefore to a final dielectric properties' reconstruction closer to the expected scenario. Moreover, we propose a new approach to compute the imaging algorithm initial guess, based on the truncated singular value decomposition technique, that appears more effective in the case of noisy measured data. Finally, the developed algorithm is applied to sets of data, measured with a microwave imaging system to reconstruct brain stroke scenarios.**

***Keywords*—microwave imaging, biomedical imaging, finite element methods, microwave antennas, electromagnetic fields, contrast source inversion method, brain stroke.**

I. Introduction

In the medical world, the microwave imaging (MWI) technique is having a growing impact both in diagnosis and therapy for different kinds of pathologies. Some examples are detection of shoulder injuries [1], monitoring of heart-beat [2] or respiration [3], breast cancer diagnosis [4]–[6]. In [7], MWI is combined with hyperthermia for cancer therapy, while, in [8], the MWI is used in order to monitor the increase of temperature in regional hyperthermia treatment, and, in [9], [10], it is combined together with ablation.

In the case of brain stroke imaging, the MWI underlying principle is based on the dielectric contrast between the brain tissues and the stroke area. Considering an ischemic stroke, which is a condition caused by the occlusion of a blood vessel, the dielectric properties of the affected area are lower than the background (healthy brain), while the hemorrhagic stroke, which is due to the rupture of a blood vessel, is characterized by dielectric properties higher than those of the background. This means that these two pathological conditions can be distinguished based on the dielectric contrast. A comprehensive review on MWI system applied to brain stroke imaging is reported in [11], which contains the last progress and provides an analysis of the benefits and limitations of this technology.

Here, to investigate the capabilities of MWI technology for brain stroke imaging, we use the MWI system described in [12] and [13]. In the used system, a fundamental role is played by the antennas that surround the head to form an helmet, acting as both transmitters and receivers. Starting from the field recovered from the antennas that surround the head, we retrieve information regarding the unknown scattering body, solving an inverse ill-posed problem. This kind of problem is usually treated via regularization methods or specific optimization procedures. In this paper, the inverse scattering problem is solved through an iterative non-linear algorithm able to quantitatively reconstruct the distribution of permittivity and conductivity in the domain of interest (DoI): the contrast source inversion (CSI) method. In the medical field, the CSI method has been also employed in combination with magnetic resonance imaging (MRI) in order to compute the distribution of the local absorption rate [14], in [5] for breast cancer diagnosis, or in [15] for the tissues dielectric properties evaluation starting from magnetic resonance data, and in other applications such as in oil industry for determining the electrical conductivity distribution between boreholes [16] or in food industry for example in detection of moisture hot-spots in grain bin as in [17]. The CSI method is, here, combined with an in-house finite element method (FEM) code [18]. After the creation of the numerical model of the scenario under test and the generation of a non-uniform, unstructured and conformal mesh composed by tetrhaedral cells, the FEM is integrated with the CSI method for the solution of the inverse problem. Besides, the whole model of the antenna together with the coaxial feeding is modeled in the geometry allowing a better estimation of the field in the DoI, but also of the scattering parameters at the ports of the antennas. Then, a novel discretization of the contrast source variables, initially proposed in [19] just with synthetic data, is here compared with the standard one via experimental data, measured with the used MWI system for cases of brain strokes. Moreover, a new approach is here presented to evaluate the initial guess of the CSI algorithm, which is a worthy alternative to the

Manuscript received xxx; revised xxx; accepted xxx. Date of publication xxx; date of current version xxx. This research was supported in part by the project PON Research and Innovation "Microwave Imaging and Detection powered by Artificial Intelligence for Medical and Industrial Applications (DM 1062/21)", in part by the project "THERAD - Microwave Theranostics for Alzheimer's Disease", funded by Compagnia di San Paolo, and in part by the Agritech National Research Center, funded by the Next-Generation EU (PNRR – MISSIONE 4 COMPONENTE 2, INVESTI- MENTO 1.4 – D.D. 1032 17/06/2022, CN00000022). *(Corresponding author: Francesca Vipiana).*

V. Mariano, J. A. Tobon Vasquez, D. O. Rodriguez-Duarte and F. Vipiana are with the Department of Electronics and Telecommunications, Politecnico di Torino, 10129 Torino, Italy (e-mail: francesca.vipiana@polito.it).

Digital Object Identifier xxxx

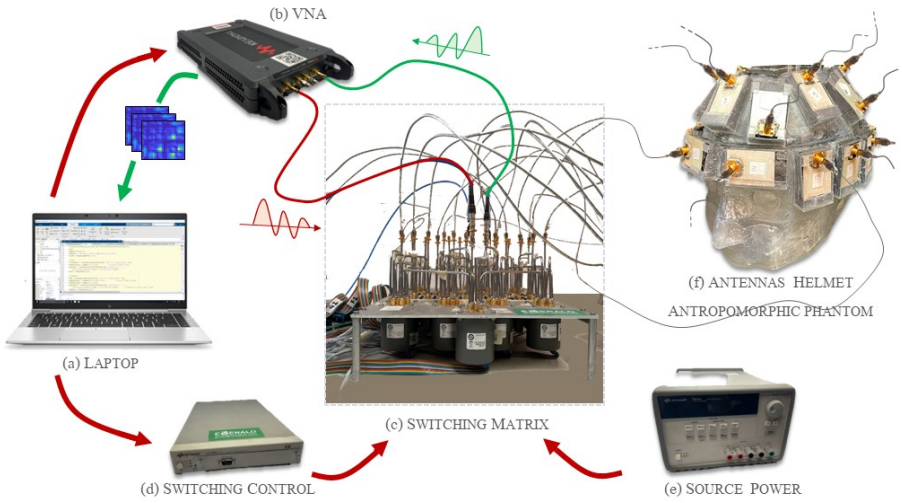

Fig. 1. Schematic overview of the MWI system and its components: (a) laptop, (b) two-ports vector network analyzers (VNA), (c) switching matrix, (d) switching control, (e) source power, (f) antennas helmet, and anthropomorphic phantom.

commonly used back-propagation technique. The paper starts with a brief description of the MWI system and of the realized anthropomorphic head phantom in Sect. II, while Sect. III contains, first, an overview of the CSI method, then the new approach to evaluate the initial guess, and finally the description of the discretizations of the contrast source variables. In Sect. IV, there are the results obtained with measured data in a realistic case of study. Finally, Sect. V contains a summary of the achieved goals and some possible future steps.

II. Microwave Imaging System and Anthropomorphic Head Phantom

The system exploited for the experimental tests is depicted in Fig. 1 with a schematic overview. The working frequency range of the system has, as central frequency, 1 GHz, as detailed in [20]. Starting from the left, there is a laptop with a script containing all the settings and the operations for the acquisition of the data. Then, there is the vector network analyser (VNA): here we use the P937XA 2-port VNA [21]. The VNA has just two ports so we need a switching matrix (in the middle of Fig. 1) enclosing all the possible path to reach the 22 antennas that surround the head. It contains electro-mechanical switches and internal interconnections, made of semi-rigid coaxial cables and designed in order to have the same length for each path from the VNA ports to the antennas, hence guaranteeing equal electric paths. It is fed by a source power and is supported by a switching control that interfaces the script with the switching matrix. On the right of Fig. 1, the anthropomorphic phantom is shown together with a helmet array of 22 flexible antennas covered by a thin layer of matching medium with a relative permittivity around 20 at 1 GHz [13]. Then, the phantom surrounded by antennas is filled with a liquid which is a mixture of 39.9% of water, 59.7% of alcohol, and 0.4% of salt, with final dielectric properties equal to a weighted average of the grey and white matter ones: $\epsilon_{\text{brain}} = 42$ and $\sigma_{\text{brain}} = 0.72$ S/m at 1 GHz. The gray and white matter dielectric properties are extrapolated from the IFAC-CNR database [22]. The phantom shape is extracted from the Visible Human Project [23] and its CAD model is shown, together with the antennas, in Fig. 2.

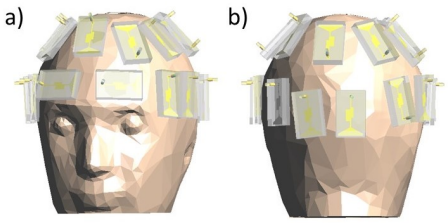

Fig. 2. CAD model of the head and the antennas: (a) front, (b) back view.

III. Contrast Source Inversion Algorithm

In this section, the exploited quantitative image reconstruction algorithm is described. To get to the core of this algorithm, the definition of the involved variables is fundamental. In all the following equations, the generic position vector in the DoI is identified with $\underline{r}$. The first variable is the dielectric contrast $\chi(\underline{r})$ between the relative complex permittivity of the background $\epsilon_b(\underline{r})$, and the scenario under test $\epsilon_r(\underline{r})$:

$$\chi(\underline{r}) \triangleq \frac{\epsilon_r(\underline{r}) - \epsilon_b(\underline{r})}{\epsilon_b(\underline{r})} \tag{1}$$

Now, considering the system in Fig. 1, one antenna at a time acts as transmitter and illuminates the DoI, while all the remaining antennas act as receivers. The field produced by the antenna t, with $t = 1, \ldots, T$ and $T = 22$, in the background scenario, is called $\underline{E}_t^{\text{inc}}(\underline{r})$, while the same variable becomes $\underline{E}_t^{\text{tot}}(\underline{r})$ in the scenario under test. The scattered field $\underline{E}_t^{\text{sct}}(\underline{r})$, produced by the presence of the target when the antenna t transmits, is simply evaluated as the difference between $\underline{E}_t^{\text{tot}}(\underline{r})$ and $\underline{E}_t^{\text{inc}}(\underline{r})$, and it is regulated by the following wave equation:

$$\nabla \times \nabla \times \underline{E}_t^{\text{sct}}(\underline{r}) - k_b^2(\underline{r})\underline{E}_t^{\text{sct}}(\underline{r}) = k_b^2(\underline{r})\chi(\underline{r})\underline{E}_t^{\text{tot}}(\underline{r}), \tag{2}$$

where $k_b(\underline{r}) = \omega\sqrt{\mu_0\epsilon_0\epsilon_b(\underline{r})}$ is the wave number in the background medium, μ_0 and ϵ_0 are the free space permeability and permittivity, and ω is the angular frequency. Looking at the right hand side of (2), we can define the so-called *contrast source* variable $\underline{\omega}_t(\underline{r})$ via the object equation:

$$\underline{\omega}_t(\underline{r}) \triangleq \chi(\underline{r})\underline{E}_t^{\mathrm{tot}}(\underline{r}). \tag{3}$$

The CSI method is an iterative algorithm based on the minimization of a cost functional $\mathcal{F}^{\mathrm{CSI}}$ by updating, at each iteration n, the values of the dielectric contrast, χ, and the contrast sources, $\underline{\omega}_t$. Before going into details of the cost function, we have to define two different domains: the domain S, that identifies the antennas' ports, and the domain D, that corresponds with the DoI which in this case is the brain. The cost functional is composed by two parts: $\mathcal{F}^{\mathrm{S}}$ that computes the error between the known measured quantity at the antennas and the one calculated at the end of each iteration, and $\mathcal{F}^{\mathrm{D}}$ that evaluates the error in the contrast sources, as follows:

$$\mathcal{F}^{\mathrm{CSI}}\left\{\chi(\underline{r}),\underline{\omega}_t(\underline{r})\right\} = \mathcal{F}^{\mathrm{S}}\left\{\underline{\omega}_t(\underline{r})\right\} + \mathcal{F}^{\mathrm{D}}\left\{\chi(\underline{r}),\underline{\omega}_t(\underline{r})\right\} \tag{4}$$

$$\mathcal{F}^{\mathrm{S}} = \frac{\sum_{t=1}^{T}\left\|\underline{E}_t^{\mathrm{sct}}(\underline{r}) - \mathcal{L}_S\{\underline{\omega}_t(\underline{r})\}\right\|_S^2}{\sum_{t=1}^{T}\left\|\underline{E}_t^{\mathrm{sct}}(\underline{r})\right\|_S^2} \tag{5}$$

$$\mathcal{F}^{\mathrm{D}} = \frac{\sum_{t=1}^{T}\left\|\chi(\underline{r})\,\underline{E}_t^{\mathrm{inc}}(\underline{r}) - \underline{\omega}_t(\underline{r}) + \chi(\underline{r})\,\mathcal{L}_D\{\underline{\omega}_t(\underline{r})\}\right\|_D^2}{\sum_{t=1}^{T}\left\|\chi(\underline{r})\,\underline{E}_t^{\mathrm{inc}}(\underline{r})\right\|_D^2}, \tag{6}$$

where the symbols $\left\|\cdot\right\|_S^2$ and $\left\|\cdot\right\|_D^2$ are the L_2-norm in the S and D domains, respectively. $\mathcal{L}_{\mathrm{S}}$ and $\mathcal{L}_{\mathrm{D}}$ are the data and domain operators, both having as input the contrast source $\underline{\omega}_t(\underline{r})$, and the output is the scattered field on S and D, respectively [24]. They are defined as:

$$\mathcal{L}_{\mathrm{X}}\{\underline{\omega}_t(\underline{r})\} = \iiint_D -k_b^2(\underline{r}')\,\underline{\omega}_t(\underline{r}')\cdot\underline{G}_b(\underline{r},\underline{r}')d^3\underline{r}' \quad \underline{r}\in \mathrm{X} \tag{7}$$

where $\mathrm{X} = \mathrm{S},\mathrm{D}$ and $\underline{G}_b(\underline{r},\underline{r}')$ is the Green's function of the considered reference scenario.

A. Initial Guess

Usually, the initial guess of the CSI algorithm is evaluated through the back-propagation method [24]; here, we propose a different procedure, based on the truncated singular values decomposition (TSVD) technique [13], exploiting the symmetry of the scattering matrix, $[S]$, due to the reciprocity of the system. As shown in Sect. IV, this approach allows to obtain a better defined initial guess if compared with the one evaluated via the classical back-propagation technique.

In the evaluation of the initial guess, we apply the Born approximation, i.e. $\underline{E}_t^{tot} \simeq \underline{E}_t^{inc}$ [25]. Now, considering a pair of antennas m and n, the differential scattering parameters $\Delta S_{m,n}$, i.e. the difference between the scattered parameters in the scenario under test with respect to the background one, can be computed applying a linear integral operator to the dielectric contrast $\chi(\underline{r})$, as shown in the following equation:

$$\Delta S_{m,n} = \frac{-j\omega\epsilon_b}{2a_m a_n}\iiint_{\mathrm{DoI}}\chi(\underline{r})\underline{E}_m^{\mathrm{inc}}(\underline{r})\cdot\underline{E}_n^{\mathrm{inc}}(\underline{r})\,d\underline{r}^3. \tag{8}$$

where a_m, a_n are the power waves at the antennas m and n. A more compact way to write (8) is:

$$\Delta S_{m,n} = \mathcal{S}\{\chi\}. \tag{9}$$

where $\mathcal{S}$ represents the integral scattering operator. Now, the TSVD method is employed to invert the discretized version of the scattering operator, and evaluate the discretized dielectric contrast, $[\chi]$, from the measured scattering parameters, as:

$$[\chi] = \sum_{l=1}^{L}\frac{1}{\sigma_l}\left\langle[\Delta S_V]^T,[u_l]\right\rangle[v_l], \tag{10}$$

where $[u_l],[v_l]$ and σ_l are the left and right singular vectors and the singular values of the discretized scattering operator, respectively. L is the threshold for the truncation of the singular values, which is chosen in order to reach a balance between the measurement inaccuracies and the information needed for the reconstruction [12]. Finally, $[\Delta S_V]$ is a column vector containing the differences between the scattering parameters measured in the scenario under test and those simulated by the FEM in the background scenario. In the following, $[\Delta S_V]$ is also represented in matrix format, $[\Delta S]$, being the rows and the columns the considered antenna pairs. The measured data has a range between -70 and -5 dB, we use an IF equal to 100 Hz in the VNA, and, since the self scattering parameters are the ones with the highest model error, we do not use them in the imaging process as in [20]. The scattering parameters are calibrated with respect to the simulated ones as described in [26], i.e. multiplying each measured scattering parameters by the ratio of the same parameter simulated and measured in a known scenario. Before applying the TSVD, the upper and lower triangular parts of $[\Delta S]$ are considered separately and symmetrized in order to obtain two different matrices, as reported in Fig. 3: $[\Delta S_U]$ and $[\Delta S_L]$. The principle is that the $[\Delta S]$ matrix has to be symmetric due to the system reciprocity: a loss of symmetry, even if very limited, represents inaccuracies in the measurements. The proposed method is used to minimize its impact in the initial guess generation for the dielectric contrast. Then, for each obtained differential scattering matrix, the dielectric contrast is evaluated via the TSVD (10), and two different values for the dielectric contrast, named $[\chi_U]$ and $[\chi_L]$, are obtained. At this point, the data are processed in order to reduce the noise and improve the quality of the initial guess. The first step is to smooth the spike and the sudden variations in the dielectric contrast distribution, substituting each value in $[\chi]$ with the average of the initial dielectric contrast values in the tetrahedra that share at least a vertex with the considered one. At the end of this operation, we have the new variables: $[\widetilde{\chi}_U]$ and $[\widetilde{\chi}_L]$. Last, the dielectric contrast initial guess is evaluated putting together the results obtained from the two triangular matrices keeping the common information only, as follows:

$$[\bar{\chi}] = \frac{|[\widetilde{\chi}_L]|}{\max(|[\widetilde{\chi}_L]|)}\cdot\frac{|[\widetilde{\chi}_U]|}{\max(|[\widetilde{\chi}_U]|)}\cdot\frac{[\widetilde{\chi}_L]+[\widetilde{\chi}_U]}{2} \tag{11}$$

where the first two terms are normalized absolute values of $[\widetilde{\chi}_U]$ and $[\widetilde{\chi}_L]$, while the last term is their mean value. Then, the discretized dielectric contrast can be assigned to any point $\underline{r}$ of DoI as:

$$\bar{\chi}(\underline{r}) = \bar{\chi}_i \;\text{ with }\; \underline{r}\in C_i \tag{12}$$

where C_i is the i-th tetrahedron and $\bar{\chi}_i$ its corresponding dielectric contrast. The dielectric contrast initial guess is:

$$\chi_0(\underline{r}) = \begin{cases} 0 & |\bar{\chi}(\underline{r})| < |\chi^T| \\ \bar{\chi}(\underline{r}) & \text{elsewhere,} \end{cases} \tag{13}$$

where χ^T is a selected percentage of the expected dielectric contrast between the healthy head and the stroke area. The kind of stroke can be determined looking at the permittivity distribution: if the target has a permittivity higher than the background, it is a hemorrhagic stroke, otherwise it is an ischemic one. The second step is the evaluation of the initial guess of the contrast source variables, $\underline{\omega}_0(\underline{r})$, through a modified object equation, i.e. using $\underline{E}_t^{\text{inc}}(\underline{r})$ instead of $\underline{E}_t^{\text{tot}}(\underline{r})$:

$$\underline{\omega}_{0,t}(\underline{r}) \triangleq \bar{\chi}_0(\underline{r})\underline{E}_t^{\text{inc}}(\underline{r}). \tag{14}$$

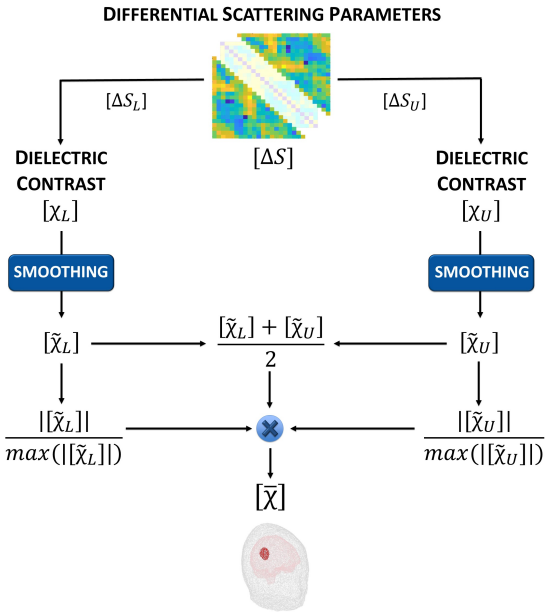

Fig. 3. Flowchart of the procedure for the initial guess evaluation.

B. Discretization of the Contrast Source Variables

This section contains the description of the two different discretizations used to implement the CSI method via the FEM solver. The proposed one is called "field-based" discretization, while the standard one is called "contrast-based". We start with the discretization of the dielectric contrast that is considered constant within each cell, so it is written as a linear combination of scalar coefficients and pulse functions:

$$\chi(\underline{r}) \cong \sum_{k=1}^{K} \chi_k \, p_k(\underline{r}), \tag{15}$$

where K is the total number of cells in the mesh, and the pulse function $p_k(\underline{r})$ is equal to 1 only within the k-th element. The electric field radiated by each antenna t is written through a linear combination of scalar coefficients and curl-conforming vector basis functions $\underline{N}_e(\underline{r})$ with $e = 1, \ldots, E$, and E is the total number of edges in the mesh [27]. The spatial domain of the function corresponds to the group of tetrahedra that share the edge e, as depicted in Fig. 4 (a). Each basis function is associated to an edge e of the discretized domain, indeed it has a constant tangential component in the edge e and no tangential component for the other edges of the tetrahedra of its domain, as shown in Fig. 5 in a 2-D triangular cell representation, for the sake of simplicity. The field can be

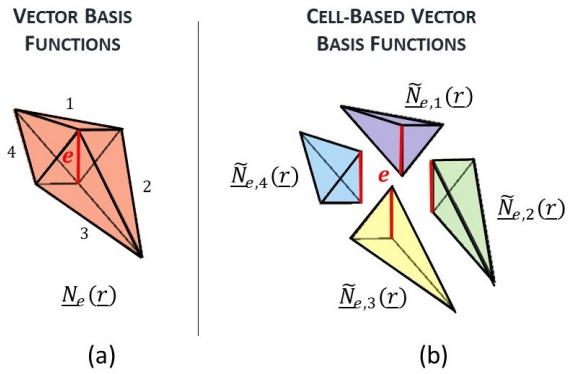

Fig. 4. Domain of definition of the vector basis functions (a), and of the cell-based vector basis functions (b).

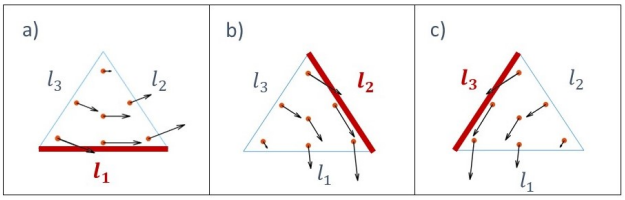

Fig. 5. Curl-conforming vectorial basis functions in a triangular element. a) Function tangential to l_1, b) function tangential to l_2, c) function tangential to l_3.

expressed via the following linear combination

$$\underline{E}_t^{\gamma}(\underline{r}) \cong \sum_{e=1}^{E} E_{t,e}^{\gamma} \, \underline{N}_e(\underline{r}), \tag{16}$$

where γ can be the total, incident or the scattered field, and $E_{t,e}^{\gamma}$ are the corresponding coefficients.

In the standard contrast-based discretization, the contrast source variable is described with the same basis functions of the dielectric contrast, i.e. the pulse functions as follows

$$\underline{\omega}_t(\underline{r}) \cong \sum_{k=1}^{K} \underline{\omega}_{t,k} \, p_k(\underline{r}), \tag{17}$$

where each *vectorial* coefficient, $\underline{\omega}_{t,k}$, is evaluated via (3), multiplying the dielectric contrast and the total field in the barycenter $\underline{r}_k$ of the tetrahedron k. Hence, as reported in Fig. 6 (a), in each point of the mesh, the contrast source variable is equal to the vector in the barycenter corresponding to the field orientation in that point. Instead, in the proposed field-based discretization, the total field is written via "cell-based" vector basis functions $\widetilde{\underline{N}}_{e,q}(\underline{r})$, which are defined starting from the previous ones via:

$$\widetilde{\underline{N}}_{e,q}(\underline{r}) = \underline{N}_e(\underline{r}) \, p_{e,q}(\underline{r}) \tag{18}$$

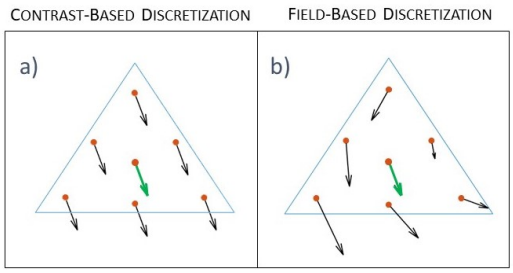

Fig. 6. Example of contrast source variable trend in a cell with the contrast-based discretization (a), or with the field-based discretization.

where $p_{e,q}$ is a pulse function equal to one only in the tetrahedron identified by the double index (e,q) and zero otherwise. The local index $q = 1,\dots,Q_e$ select one of the tetrahedra sharing the edge e. In this case, the vector basis function $\underline{\widetilde{N}}_{e,q}(\underline{r})$ has a domain corresponding only with the tetrahedron (e,q), as reported in Fig. 4 (b). In the proposed discretization, the field in (16) is rewritten using the cell-based vector basis functions (18) as:

$$\underline{E}_t^{\text{tot}}(\underline{r}) \cong \sum_{e=1}^{E} E_{t,e}^{\text{tot}} \sum_{q=1}^{Q_e} \underline{N}_e(\underline{r}) p_{e,q}(\underline{r}) = \sum_{e=1}^{E} \sum_{q=1}^{Q_e} E_{t,e}^{\text{tot}} \underline{\widetilde{N}}_{e,q}(\underline{r}) \tag{19}$$

Now, we can write the formulation of the contrast source substituting (15) and (19) in (3) as below:

$$\begin{aligned} \underline{\omega}_t(\underline{r}) &\cong \left[\sum_{k=1}^{K} \chi_k \, p_k(\underline{r})\right] \left[\sum_{e=1}^{E} \sum_{q=1}^{Q_e} E_{t,e}^{\text{tot}} \underline{\widetilde{N}}_{e,q}(\underline{r})\right] \\ &= \sum_{e=1}^{E} E_{t,e}^{\text{tot}} \sum_{k=1}^{K} \sum_{q=1}^{Q_e} \chi_k \, p_k(\underline{r}) \underline{\widetilde{N}}_{e,q}(\underline{r}). \end{aligned}$$

Since the index k and the double index (e,q) identify both an element in the mesh, we can merge them using the (e,q) one also for the dielectric contrast and the pulse function:

$$\begin{aligned} \underline{\omega}_t(\underline{r}) &\cong \sum_{e=1}^{E} E_{t,e}^{\text{tot}} \sum_{q=1}^{Q_e} \chi_{e,q} p_{e,q}(\underline{r}) \, \underline{\widetilde{N}}_{e,q}(\underline{r}) \\ &= \sum_{e=1}^{E} \sum_{q=1}^{Q_e} \omega_{t,e,q} \, \underline{\widetilde{N}}_{e,q}(\underline{r}). \end{aligned} \tag{20}$$

where $\omega_{t,e,q} = E_{t,e}^{\text{tot}} \, \chi_{e,q}$, and, since the domain of the function $\underline{\widetilde{N}}_{e,q}(\underline{r})$ is already bounded to the element (e,q), the pulse function $p_{e,q}$ is useless and hence removed. In this case, the contrast source $\underline{\omega}_t(\underline{r})$ is written as a linear combination of the vectorial basis functions of the field via *scalar* coefficients. In this way, the contrast source keeps the same trend of the field, as evident in Fig. 6 (b), and its value can change in any cell point. Moreover, the proposed formulation simplifies the implementation of the algorithm, in fact, since the contrast source and the field are written with the same basis, the update of the variables are just done considering the scalar coefficients, therefore the algorithm uses only scalar variables and scalar operators, and does not need the dyadic operators used in the contrast-based discretization [24].

IV. Experimental Results

In this section, the CSI method is applied to the data measured with the MWI system described in Sect. II. The pathological cases are created inserting a stroke phantom in the head case, in different positions. Figure 7 (b) shows the structure exploited during the experimental tests for the positioning of the stroke phantom, reported in Fig. 7 (c), in the head phantom, as depicted in Fig. 7 (a), which contains the realized mixture (Sect. II). The upper part of the structure in Fig. 7 is created in order to perfectly match the hole in the head phantom. The stroke balloon is filled with a mixture composed of water (66.4%), alcohol (33.0%), and salt (0.6%), that has the same dielectric properties of the blood: $\epsilon_{\text{blood}} = 63.29$ and $\sigma_{\text{blood}} = 1.63$ S/m at 1 GHz [22].

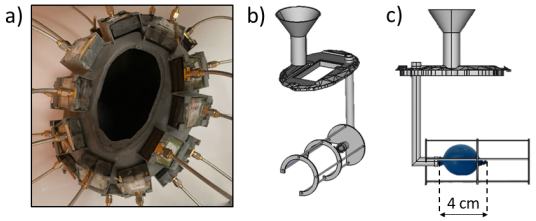

Fig. 7. Phantoms: (a) upper view of the head phantom, (b) structure used to position the balloon in the head phantom, (c) structure with the balloon.

In the following, we report the results obtained with two study cases: stroke in the back-left (BL) side of the head and in the middle-right (MR). Both the cases have a distance from the top of the head phantom equal to 7.5 cm, while the distance from the axis that divides the two brain hemispheres is equal to 2.5 cm for the BL case, and to 2.0 cm for the MR case. The chosen number of iterations in the CSI is limited 100, as a trade-off between the quality of the final reconstructions and the time to achieve them [19]; each iteration takes around 7 minutes in our implementation using an Intel(R) Xeon(R) Silver 4116 CPU @ 2.10 GHz, 24 cores. In all the considered cases, the corresponding cost function has a monotonic decreasing behavior. Before going to the obtained final reconstruction, Fig. 8 shows the permittivity distribution of the initial guess obtained with the standard back-propagation (a), and with the proposed TSVD-based technique (b), which is able to better identify the stroke area. In this case, the threshold χ^T (13) is equal to 0.06, which corresponds to the 10% of the dielectric contrast between the background and the hemorrhagic stroke region that is highlighted in the reconstruction images with a white line.

The initial guess is one of the fundamental steps of the CSI algorithm, indeed it strongly affects the final result: if the initial guess does not contain enough information, the final reconstruction does not converge to the expected scenario. Since, in this case, the back-propagation does not detect any stroke in the initial guess, as evident in Fig. 8 (a), the CSI method is not able to reconstruct the stroke. Hence, we show only the final results obtained using the initial guess evaluated via the TSVD-based technique reported in Fig. 8 (b). Figure 9 shows the permittivity reconstruction in the three main cuts for the two discretizations in the BL case: in Fig. 9 (a) the contrast-

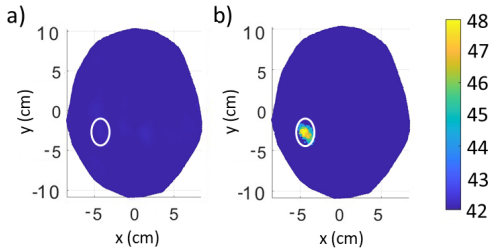

Fig. 8. Permittivity distribution of the initial guess: (a) back-propagation and (b) TSVD-based technique.

based discretization and in Fig. 9 (b) the field-based one. Also, the conductivity distributions are reported in Fig. 10. We can observe that the field-based discretization is able to reach higher values in the stroke region. Besides, the reconstruction with the contrast-based discretization is more discontinuous, indeed the "dotted" distribution of the permittivity and conductivity is probably due to the worse resolution of the discretization. In the second case of study (MR), for the sake

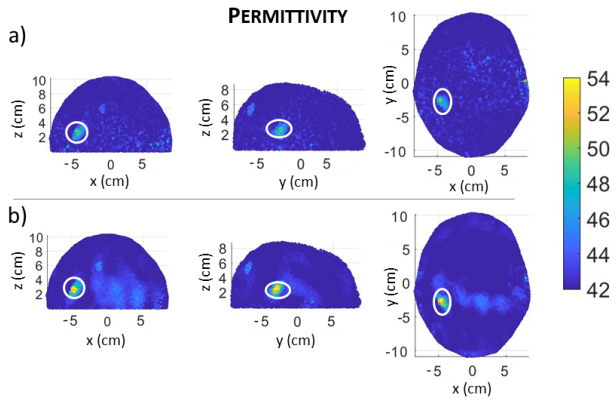

Fig. 9. Permittivity distribution in the 3 main cuts. Back-left case after 100 iterations with the contrast-based (a), and the field-based discretization (b).

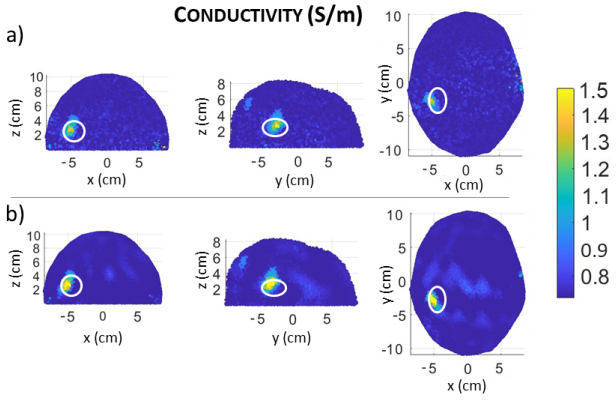

Fig. 10. Conductivity distribution in the 3 main cuts. Back-left case after 100 iterations with the contrast-based (a), and the field-based discretization (b).

of brevity, we report the xy-plane view only: in Fig. 11 (a) and (c) there are permittivity and conductivity reconstructions with the contrast-based discretization, respectively, while 11 (b) and (d) with the field-based discretization. Even in this case, the field-based discretization reaches higher values in the stroke region, and the reconstruction appears smoother than the one obtained with the contrast-based dicretization. Comparing the BL case with the MR one, it is evident that the dielectric properties values in the stroke region obtained in the BL case are closer to the expected ones. Probably, this is due to the antennas configuration in the helmet: in the back-side a better coverage is expected with respect to the front-side (Fig. 2).

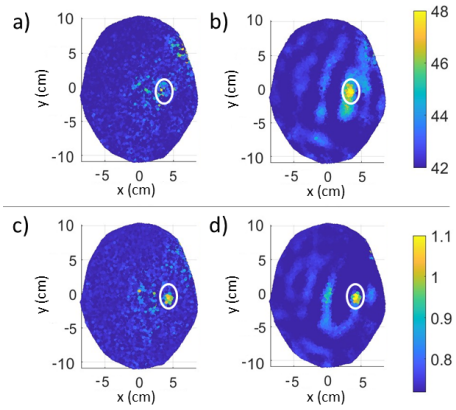

Fig. 11. Middle-right case after 100 iterations: a) permittivity, c) conductivity distribution with contrast-based; b) and d) with field-based discretization.

V. Conclusion and Perspectives

In this work, an innovative way to discretize the variables in the CSI algorithm is exploited for the brain stroke reconstruction using a MWI system. In the proposed field-based discretization, the contrast source variables have a linear variation within each tetrahedral cell. This feature allows to reach reconstructed dielectric properties in the stroke area closer to the expected ones if compered with the standard contrast-based discretization. Moreover, at the beginning of the CSI algorithm, we applied a customized technique for the evaluation of the initial guess that is based on the TSVD approach and exploits the reciprocity of the MWI system. This method allows to obtain better initial guesses, and therefore improved final results. With the proposed implementation, the CSI algorithm is able, with the measured scattering parameters, to recognize the stroke position and shape, and get stroke dielectric properties close to the expected ones. Next steps of this work regard the application of the algorithm to an extensive set of measured data in order to understand its behavior with different cases of study, i.e. strokes of different sizes, positions and also different type (ischemic), and then, the use of a more realistic multi-tissue head phantom as described in [28], [29]. Moreover, a possible implementation change that could improve the performance is using a finer mesh for the fields' evaluation in the whole domain via the forward model, and a coarser mesh for the operator exploited in the solution of the inverse problem. Finally, in order to speed up the time to achieve the final results, a method that can be used is the one described in [30], [31], in which the domain under test is decomposed in smaller subproblems particularly suitable for parallel computing.

REFERENCES

[1] S. Borzooei, P.-H. Tournier, C. Migliaccio, V. Dolean, and P. Christian, "Microwave tomographic imaging of shoulder injury," in *Conférence EUCAP 2023*, IEEE, Ed., Florence, Italy, Mar. 2023, p. 5. [Online]. Available: https://hal.science/hal-04056885

[2] S. El-Samad, D. Obeid, G. Zaharia, S. Sadek, and G. Zein, "Heartbeat rate measurement using microwave systems: single-antenna, two-antennas, and modeling a moving person," *Analog Integrated Circuits and Signal Processing*, vol. 96, 08 2018.

[3] M. Zakrzewski, H. Raittinen, and J. Vanhala, "Comparison of center estimation algorithms for heart and respiration monitoring with microwave doppler radar," *IEEE Sensors Journal*, vol. 12, no. 3, pp. 627–634, 2012.

[4] D. Tajik, F. Foroutan, D. S. Shumakov, A. D. Pitcher, and N. K. Nikolova, "Real-time microwave imaging of a compressed breast phantom with planar scanning," *IEEE Journal of Electromagnetics, RF and Microwaves in Medicine and Biology*, vol. 2, no. 3, pp. 154–162, 2018.

[5] C. Kaye, I. Jeffrey, and J. LoVetri, "Improvement of multi-frequency microwave breast imaging through frequency cycling and tissue-dependent mapping," *IEEE Transactions on Antennas and Propagation*, vol. 67, no. 11, pp. 7087–7096, 2019.

[6] M. Lu, X. Xiao, Y. Pang, G. Liu and H. Lu, "Detection and Localization of Breast Cancer Using UWB Microwave Technology and CNN-LSTM Framework," *IEEE Transactions on Microwave Theory and Techniques*, vol. 70, no. 11, pp. 5085–5094, 2022.

[7] M. Ghaderi Aram, L. Beilina, and H. Dobsicek Trefna, "Microwave thermometry with potential application in non-invasive monitoring of hyperthermia," *Journal of Inverse and Ill-posed Problems*, vol. 28, no. 5, pp. 739–750, 2020.

[8] A. Yago Ruiz, M. Cavagnaro, and L. Crocco, "Hyperthermia treatment monitoring via deep learning enhanced microwave imaging: A numerical assessment," *Cancers*, vol. 15, no. 6, 2023. [Online]. Available: https://www.mdpi.com/2072-6694/15/6/1717

[9] A. L. Evans, J. F. Sawicki, H. Luyen, Y. Mohtashami, N. Behdad, and S. C. Hagness, "Feasibility study of microsecond pulsed microwave ablation using a minimally invasive antenna," *IEEE Antennas and Wireless Propagation Letters*, vol. 20, no. 4, pp. 627–631, 2021.

[10] M. Wang, R. Scapaticci, M. Cavagnaro, and L. Crocco, "Towards a microwave imaging system for continuous monitoring of liver tumor ablation: Design and in silico validation of an experimental setup," *Diagnostics*, vol. 11, no. 5, 2021. [Online]. Available: https://www.mdpi.com/2075-4418/11/5/866

[11] L. Guo, A. S. M. Alqadami, and A. Abbosh, "Stroke diagnosis using microwave techniques: Review of systems and algorithms," *IEEE Journal of Electromagnetics, RF and Microwaves in Medicine and Biology*, vol. 7, no. 2, pp. 122–135, 2023.

[12] D. O. Rodriguez-Duarte, J. A. Tobon Vasquez, R. Scapaticci, G. Turvani, M. Cavagnaro, M. R. Casu, L. Crocco, and F. Vipiana, "Experimental validation of a microwave system for brain stroke 3-D imaging," *Diagnostics*, vol. 11, no. 7, p. 1232, 2021.

[13] D. O. Rodriguez-Duarte, C. Origlia, J. A. T. Vasquez, R. Scapaticci, L. Crocco, and F. Vipiana, "Experimental assessment of real-time brain stroke monitoring via a microwave imaging scanner," *IEEE Open Journal of Antennas and Propagation*, vol. 3, pp. 824–835, July 2022.

[14] A. Arduino, L. Zilberti, M. Chiampi, and O. Bottauscio, "CSI-EPT in presence of RF-shield for MR-coils," *IEEE Transactions on Medical Imaging*, vol. PP, pp. 1–1, 02 2017.

[15] R. L. Leijsen, W. M. Brink, C. A. T. van den Berg, A. G. Webb and R. F. Remis, "3-D Contrast Source Inversion-Electrical Properties Tomography," *IEEE Transactions on Medical Imaging*, vol. 37, no. 9, pp. 2080-2089, Sept. 20185.

[16] A. Abubakar and P. van den Berg, "Three-dimensional inverse scattering applied to cross-well induction sensors," *IEEE Transactions on Geoscience and Remote Sensing*, vol. 38, no. 4, pp. 1669–1681, 2000.

[17] A. Zakaria, I. Jeffrey, and J. LoVetri, "Full-vectorial parallel finite-element contrast source inversion method," *Progress In Electromagnetics Research*, vol. 142, pp. 463–483, 01 2013.

[18] D. O. Rodriguez-Duarte, J. A. Tobon Vasquez, R. Scapaticci, L. Crocco, and F. Vipiana, "Assessing a microwave imaging system for brain stroke monitoring via high fidelity numerical modelling," *IEEE J. Electromagn., RF, Microw. Med. Biol.*, pp. 1–1, 2021.

[19] V. Mariano, J. A. Tobon Vasquez, and F. Vipiana, "A novel discretization procedure in the CSI-FEM algorithm for brain stroke microwave imaging," *Sensors*, vol. 23, no. 1, 2023. [Online]. Available: https://www.mdpi.com/1424-8220/23/1/11

[20] J. A. Tobon Vasquez, R. Scapaticci, G. Turvani, G. Bellizzi, D. O. Rodriguez-Duarte, N. Joachimowicz, B. Duchêne, E. Tedeschi, M. R. Casu, L. Crocco, and F. Vipiana, "A prototype microwave system for 3D brain stroke imaging," *Sensors*, vol. 20, no. 9, 2020. [Online]. Available: https://www.mdpi.com/1424-8220/20/9/2607

[21] Keysight Technologies, "Keysight streamline series USB vector network analyzer P937XA 2-port, up to 26.5 GHz," *Data Sheet*, Oct. 2018.

[22] D.Andreuccetti, R.Fossi, and C.Petrucci, "An internet resource for the calculation of the dielectric properties of body tissues in the frequency range 10 Hz - 100 GHz. IFAC-CNR, Florence (Italy), 1997. Based on data published by C.Gabriel et al. in 1996." Accessed on: Feb. 28, 2020. [Online]. Available: http://niremf.ifac.cnr.it/tissprop/.

[23] S. N. Makarov, G. M. Noetscher, J. Yanamadala, M. W. Piazza, S. Louie, A. Prokop, A. Nazarian, and A. Nummenmaa, "Virtual human models for electromagnetic studies and their applications," *IEEE Reviews in Biomedical Engineering*, vol. 10, pp. 95–121, 2017.

[24] A. Zakaria, *The finite-element contrast source inversion method for microwave imaging applications*. University of Manitoba (Canada), 2012.

[25] R. Scapaticci, J. Tobon, G. Bellizzi, F. Vipiana, and L. Crocco, "Design and numerical characterization of a low-complexity microwave device for brain stroke monitoring," *IEEE Transactions on Antennas and Propagation*, vol. 66, no. 12, pp. 7328–7338, 2018.

[26] C. Gilmore, P. Mojabi, A. Zakaria, M. Ostadrahimi, C. Kaye, S. Noghanian, L. Shafai, S. Pistorius, and J. LoVetri, "A wideband microwave tomography system with a novel frequency selection procedure," *IEEE Transactions on Biomedical Engineering*, vol. 57, no. 4, pp. 894–904, 2010.

[27] J. Jin, "The finite element method in electromagnetics," New York: Wiley, 2002.

[28] C. Origlia, M. Gugliermino, D. O. Rodriguez-Duarte, J. A. Tobon Vasquez, and F. Vipiana, "Anthropomorphic multi-tissue head phantom for microwave imaging devices testing," in *2023 17th European Conference on Antennas and Propagation (EuCAP)*, 2023, pp. 1–4.

[29] D. O. Rodriguez-Duarte et al., "Brain Stroke Monitoring via a Low-complexity Microwave Scanner: Realistic Multi-tissue Head Phantom Validation," in *2023 IEEE Conference on Antenna Measurements and Applications (CAMA)*, 2023, pp. 116–119.

[30] P. H. Tournier, et al., "Numerical Modeling and High-Speed Parallel Computing: New Perspectives on Tomographic Microwave Imaging for Brain Stroke Detection and Monitoring," in *IEEE Antennas and Propagation Magazine*, vol. 59, no. 5, pp. 98–110, 2017.

[31] J. Lu, Y. Chen, D. Li and J. -F. Lee,, "An Embedded Domain Decomposition Method for Electromagnetic Modeling and Design," in *IEEE Transactions on Antennas and Propagation*, vol. 67, no. 1, pp. 309–323, 2019.

Valeria Mariano completed the Bachelor and the Master's degree (summa cum laude) in Biomedical Engineering with a specialization in medical instrumentation at the Politecnico di Torino, Torino, Italy, in 2017 and in 2019, respectively. She received the Ph.D. degree (summa cum laude) in Electronics and Telecommunication Engineering from the Politecnico di Torino, in 2023. In 2022, she was a visiting researcher in the University of Manitoba, Winnipeg, Canada. She works now at Politecnico di Torino as a post-doc researcher. She received the TICRA Travel Grant at the International Symposium on Antennas and Propagation and USNC-URSI A Radio Science Meeting in 2022. Her research activity is focused on the data processing and software implementation of deterministic algorithms and machine learning-based algorithms for the development of a microwave imaging device for brain stroke diagnosis.

Jorge Tobon (Member, IEEE) received the Degree in electronics engineering from the Universidad de Antioquia, Colombia, in 2010, in a double degree program, the master's degree in electronic engineering and the Ph.D. degree in electronics and telecommunication engineering from the Politecnico di Torino, Italy, in 2010 and 2014, respectively, where he is an Assistant Professor. His main research activities correspond to modeling, designing, and analyzing systems for microwave imaging applications, specifically in the biomedical and food industry fields, and the numerical modeling of complex and nonhomogeneous media propagation. He received the "Premio Latmiral," an award granted by the Italian Society of Electromagnetism in 2018 and the URSI General Assembly Scientific Symposium Young Scientist Award and the Sorrentino URSI Italy National Meeting Young Scientist Paper Award in 2020.

David Rodriguez is an assistant professor at the Department of Electronics and Telecommunications at Politecnico di Torino, Italy, where he received his Ph.D. degree (summa cum laude) in 2022. He completed his B.Sc. and M.Sc. degrees in electronic engineering from Universidad Nacional de Colombia in 2013 and 2018. Currently, his focus is on applied electromagnetics to biomedical and agro-industrial problems. He is a mentor in the 2023 IEEE EMBS and 2024 European Association on Antennas and Propagation (EurAAP) Mentorship Programs. He has been a Marie Sklodowska-Curie Early-Stage-Research Fellow as part of the European project EMERALD, being a visiting researcher in WIPL-D, Serbia, iLumens-Health Simulation Center, France, and Keysight, Austria. In 2015, he collaborated with the Control and Energy Nanosatellites group at Universidad Sergio Arboleda, Colombia. In 2017, he was a visiting researcher at the University of British Columbia, Okanagan, Canada, funded by the Emerging Leaders in the Americas Program (ELAP). Dr. Rodriguez-Duarte received the IEEE Antennas and Propagation Society Postdoctoral Fellowship (APSF) in 2022 and was awarded the best undergraduate thesis of the electronics department in 2013, the Second Prize in the Student Paper Competition in the 2021 URSI General Assembly Scientific Symposium (GASS), the AP-S Tapan Sarkar Best Student Paper in 2021 IEEE International Conference on Antenna Measurements and Applications (CAMA), the C. J. Reddy Travel Grant for Graduate Students in IEEE AP-S/URSI 2021, the best Propagation Paper finalist in the 2022 European Conference on Antennas (EuCAP2022), the Young Scientist Award (YSA) at the URSI combined Atlantic/Asia-Pacific Radio Science Conference (AT-AP-RASC) in 2022, and finalist for Young Scientist Award (YSA) at 2023 URSI Spain National Symposium.

Francesca Vipiana (M'07–SM'13) received the Laurea and Ph.D. degrees in electronic engineering from the Politecnico di Torino, Torino, Italy, in 2000 and 2004, respectively, with doctoral research carried out partly at the European Space Research Technology Center, Noordwijk, The Netherlands. From 2005 to 2008, she was a Research Fellow with the Department of Electronics, Politecnico di Torino. From 2009 to 2012, she was the Head of the Antenna and EMC Laboratory, Istituto Superiore Mario Boella, Torino. Since 2012, she has been an Assistant Professor with the Department of Electronics and Telecommunications, Politecnico di Torino, where she has been an Associate Professor since 2014 and a Full Professor since 2021. Her current research interests include the modelling, design and testing of microwave imaging systems for medical and industrial applications. Moreover, she is currently involved in the development of numerical techniques based on integral equation and method of moment approaches, with a focus on multiresolution and hierarchical schemes, domain decomposition, preconditioning and fast solution methods, and advanced quadrature integration schemes. She received the Young Scientist Award at the URSI General Assembly in 2005, the First Prize in the Poster Competition at the IEEE Women in Electromagnetics Workshop in 2009, the ISMB Best Paper Award in 2011, the Lot Shafai Mid-Career Distinguished Award from the IEEE Antennas and Propagation Society in 2017, and the INDRA Best Paper Award at the XXXVIII Spanish National URSI Symposium in 2023. She is also on Editorial Board of the IEEE Transactions on Antennas and Propagation and IEEE Antennas and Propagation Magazine.